Garcia Nunez, C. , Navaraj, W. T., Liu, F., Shakthivel, D. and Dahiya, R. (2018) Large-area self-assembly of silica microspheres/nanospheres by temperature-assisted dip-coating. *ACS Applied Materials and Interfaces*, 10(3), pp. 3058-3068. (doi:10.1021/acsami.7b15178)

This is the author's final accepted version.

There may be differences between this version and the published version. You are advised to consult the publisher's version if you wish to cite from it.

http://eprints.gla.ac.uk/154613/

Deposited on: 03 January 2018

Enlighten – Research publications by members of the University of Glasgow
http://eprints.gla.ac.uk

1
2
3
4
5
6
7
8
9
10
11
12
13
14
15
16
17
18
19
20
21
22
23
24
25
26
27
28
29
30
31
32
33
34
35
36
37
38
39
40
41
42
43
44
45
46
47
48
49
50
51
52
53
54
55
56
57
58
59
60

Large-area Self-assembly of Silica Micro/nanospheres by Temperature-assisted Dip-coating

*Carlos García Núñez, William Taube Navaraj, Fengyuan Liu, Dhayalan Shakthivel and Ravinder Dahiya**

Bendable Electronics and Sensing Technologies, School of Engineering,

University of Glasgow, G12 8QQ Glasgow, United Kingdom (UK)

Keywords: dip-coating, self-assembly, colloidal suspensions, photovoltaics, nanowires.

Abstract

This work reports a temperature-assisted dip-coating method for self-assembly of silica (SiO_2) micro-/nano-spheres (SPs) as monolayers over large areas (~cm^2). The area over which self-assembled monolayers (SAMs) are formed can be controlled by tuning the suspension temperature (T_s), which allows precise control over meniscus shape. Furthermore, the formation of periodic stripes of SAM, with excellent dimensional control (stripe width and stripe-to-stripe

spacing), is demonstrated using a suitable set of dip-coating parameters. These findings establish the role of T_s, and other parameters such as withdrawal speed (V_w), withdrawal angle (θ_w) and withdrawal step length (L_w). For T_s ranged between 25-80°C, the morphological analysis of dip-coatings shows layered structures comprising of defective layers (25-60°C), single layers (70°C), and multi-layer (>70°C) owing to the variation of SPs flux at the meniscus/substrate assembling interface. At T_s= 70°C, there is an optimum V_w, approximately equal to the downshift speed of the meniscus (V_m =1.3 μm/s), which allows the SAM formation over areas (2.25 cm^2) roughly 10 times larger than reported in literature using nanospheres. Finally, the large-area SAM is used to demonstrate the enhanced performance of anti-reflective coatings for photovoltaic cells, and to create metal nano-mesh for Si nanowire synthesis.

1. Introduction

The large-area self-assembly of micro-metric and sub-micrometric particles with the shape of spheres (SPs) can impart new functionalities to surfaces by modifying their wettability, optical reflectivity, tribological properties, hardness, conductivity, etc.[1-6] Self-assembled monolayers (SAMs) based on organic and inorganic SPs have been demonstrated to be promising for the development of a wide variety of applications, including photonics,[7-8] photovoltaics (PVs),[9] smart-coatings[10] and sensing.[11-12] Metallic SPs SAMs is another attractive route which offers solutions for closed-compact porous coatings for catalytic support during the synthesis of various nanostructures such as semiconducting nanowires (NWs).[13-15] Porous metallic layers exhibiting enhanced electromagnetic transmission due to the surface plasmonic resonance[16] are attractive for the development of novel lithographic and optical applications.[17] The assembly and ordering

of these organic and inorganic SPs on various substrates[18] can be obtained using techniques such as dip-coating,[19-20] drop-casting,[21] spin-coating,[22-23] Langmuir-Blodgett (LB),[24-26] sedimentation,[27] confined convective assembly[15, 28-30] capillary forces based assembly,[31] vertical deposition,[32] scalable printing,[33] dielectrophoresis,[34] and forced filtration[35]. **Table 1** provides a comparison of these techniques. It may be noted from **Table 1** that LB[24] and charge reversible substrates[18] exhibit record surface coverages of silica (SiO_2) SPs SAM (around 63-64 cm^2). However, the mechanism governing these processes requires the surface functionalization of SPs (or substrate).[24-25] In this regard, dip-coating is interesting as it does not require any chemical pre-treatment of the SPs surface and reduces the complexity while showing similar outcome in terms of large area assembly of SPs. Surprisingly, this technique has not been extensively explored for large-area coatings of micron and sub-micron particles. The advantage of the work reported here, with respect to conventional dip-coating procedures,[19-20] include the larger micro/nanospheres SAM surface coverages and better control over the SPs SAM stripe-pattern morphology by using temperature-assisted dip-coating approach (see **Table 1**).

The mechanism governing dip-coating process is known as convective assembly[36] and has features similar to those observed in three-dimensional (3D) colloidal crystals obtained in particle assembly in slits between solid plates.[37] In dip-coating method, SPs are assembled on the substrate surface by dipping the substrate in the colloidal suspension and slowly withdrawing the substrate from the suspension, or keeping the substrate position and evaporating the solvent.[19] In the latter case, the relatively low volume fraction of colloids, in comparison to the solvent volume which need to be evaporated, requires large process times and consumes relatively high energy. Moreover, SPs tend to attach not only to the surface of substrate but also to the reservoir walls, reducing the effective incorporation of particles on the substrate, thus making the process

costly and hindering the control over the process. From most relevant works about dip-coating of SPs,[2, 19-20, 29] it may be noted that parameters such as withdrawal conditions (speed, angle, and length), solution properties (SPs concentration and temperature), substrate immersion time, substrate properties (material and pre-treatments), and relative humidity of the ambient etc. that govern the optimal assembly conditions to form highly ordered and closely packed SAM of SPs are still not well understood. In this regard, the work by Wang et al.,[20] is worth noting as they show a preliminary study about the influence of some of aforementioned parameters on the spatial extension and structure of SiO_2 SPs SAM. This study show that the SAM surface coverage can be increased by increasing the SPs concentration in the colloidal solution (5-27 wt%), the withdrawal speed (0.11-3.53 mm/s), the immersion time in the solution (1-4 min) or using a relatively low humidity ambient (20-50%). However, further understanding of above parameters as well as others that have not been thoroughly investigated (e.g. SPs solution temperature, substrate pre-treatment, withdrawal angle, withdrawal step, and SPs size) is needed for the development of high-performance large-area electronic applications such as smart windows, photovoltaics, robotic e-skin, and wearable systems etc.[9-10, 38-45] These applications often use nanostructures as building blocks and therefore this work presents the enabling comprehensive study.

In this work, we have studied the influence of SPs suspension temperature (T_s) on the formation of SAMs SiO_2 micro- and nano-SPs over large areas. The SAM surface coverage is analysed as a function of the substrate withdrawal speed (V_w), angle (θ_w), length (L_w), colloidal suspension concentration and SPs average diameter (d_{SP}). As potential applications, we show the use of large-area SiO_2 SPs SAM as anti-reflective coating (ARC) in PV cells and as micrometric mask

for the deposition of porous metallic coatings for the metal-assisted chemical etching (MACE) synthesis of Si NWs.

2. Experimental Section

2.1. Silica Spheres Suspension

Aqueous monodisperse SiO_2 SPs with average diameters of 100 nm, 500 nm and 1 μm, and standard deviation (SD) of 5, 13 and 26 nm, respectively, and a SPs weight concentration (w/v) of 5% (from Microspheres-Nanospheres) have been used in this work. Stability of the suspension with time plays a critical role in the performance of dip coating. UV-Vis-NIR transmission spectroscopy has been used to characterize SPs of variation concentration and with time. Transmittance (*T*) of suspensions with various w/v has been measured overtime (**Figure 1**). Initial w/v has been diluted by adding different volumes of deionized (DI) water –obtained from a reserve osmosis system (Elix)– resulting in SPs suspension with w/v of 2.5, 1.25, 0.63 and 0.31%. **Figure 1** shows *T* of SPs suspension measured by ultraviolet/visible (UV/VIS) spectrophotometry (UV2600 Shimadzu) at wavelengths (λ) ranged between 200 and 1300 nm. For the sake of clarity, baseline corresponding to the *T* of DI water, i.e. w/v of 0%, is also included in **Figure 1**(a). Prior to the optical characterization, each suspension is sonicated for 5 min using a probe sonicator from CamSonix, resulting in a stable suspension with high uniform distribution of SPs along the entire suspension volume. This trend is further confirmed in the inset of **Figure 1**(a), where *T* –measured e.g. at λ of 1144 nm– is represented as a function of SPs w/v.

The stability of a 0.5 μm SPs suspension with a w/v of 5% has been characterized by measuring its transmittance spectrum overtime. **Figure 1**(b) shows spectral *T* for λ ranging between 200 and 1300 nm (Inset: enlarge spectrum with λ between 925 and 1050 nm) measured overtime.

1 2 3 4 5 6 7 8 9 10 11 12 13 14 15 16 17 18 19 20 21 22 23 24 25 26 27 28 29 30 31 32 33 34 35 36 37 38 39 40 41 42 43 44 45 46 47 48 49 50 51 52 53 54 55 56 57 58 59 60

From this figure, it can be observed that the SPs suspension is stable overtime, exhibiting a low variation of T, i.e. ΔT below 2.5% up to 6 h (see inset of **Figure 1**(b)). Inset of **Figure 1**(b) also includes the expression used to calculate ΔT.

2.2. Receiver Substrate Preparation

The 1.5×1.5 cm^2 pieces of prime grade and single side polished p-type <100> Si wafers, with roughness below 1.5 nm, and resistivity of 1-10 Ωcm, are used as the receiver substrates for dip-coating. Prior to the dip-coating process, native oxide is removed from Si surface by dipping the samples in a low-concentrated HF oxide-etch solution (5:1 buffered oxide etchant, which gives an etching rate of 100 nm/min). After 2 min of HF etching process, the substrate is thoroughly rinsed with DI water and dried under N_2 flow. Thereafter, the substrate is immersed in a piranha solution (H_2SO_4:H_2O_2 in volume ratio of 3:1) for 10 min to remove any organic surface contaminants and to make the surface highly hydrophilic. Again, the substrate is thoroughly rinsed with DI water and dried under N_2 flow. Finally, the substrate is exposed to an O_2 plasma (Oxygen Barrel Asher) at 150 W, using 25 sccm O_2 flux for 4 min to hydroxylate the surface of Si, i.e. to create a uniform coverage of -OH group over the entire Si substrate surface. The contact angle measurements demonstrate hydrophobicity (see **Figure S-1**(a)) and hydrophilicity (see **Figure S-1**(b)) of Si substrates after HF and O_2 plasma treatments, respectively.

2.3. Dip-coating Procedure

Figure 2 shows a 2D schematic illustration of the custom-made setup built for the dip-coating process. The set-up permits control over different operational parameters, including receiver substrate withdrawal speed (V_w), withdrawal step (L_w), withdrawal angle (θ_w) and temperature of the SPs suspension (T_s). Briefly, the withdrawal parameters determine the pulling conditions of the receiver substrate, with: i) V_w measured in μm/s setting the pulling speed of the receiver substrate from the SPs solution; ii) L_w measured in length units determining the stroke of pulling

step which can cover lengths above or below sample lengths for uniform coatings of receiver substrate (see Sections 3.1-3.2), and for strip-pattern based coatings (see Section 3.5), iii) θ_w measured in degrees setting the pulling angle of receiver substrate with respect to pulling direction (see Section 3.3). The whole setup has been placed inside a custom-made humidity chamber, consisting of a cube of acrylic glass with silicone shield at edges, to enhance the reproducibility of the process by preventing air convective effects. Both, temperature and RH of the environment have been measured *in-situ* using a digital hygrometer from Farnell (HTD-625). The top side of the chamber was modified by drilling a distribution of holes to reduce the RH of chamber down to constant values of around 20%. The use of a low RH allows the evaporation of solvent from SPs solution at rates in the range of 0.1-10 μm/s, which is approximately in the range of speeds that will be used to withdraw the receiver substrate. In addition, the humidity chamber has been placed on top of an optical table (from Newport) to prevent any external vibration during the dip-coating experiments.

Prior to the dip-coating process, the SPs suspension is sonicated for 5 min and heated up to temperatures ranging between 25°C (room temperature, RT) and 80°C. The suspension is heated by using a hot plate (Stuart, CD162) with a polytetrafluoroethylene (PTFE)-coated temperature probe for good control over T_s. Then, a hydroxylated Si substrate is vertically attached to a 3D printed platform – forming a θ_w of 0° – which is driven by a linear motor (VT-21 Linear Stage from Micronix USA) controlled by LabVIEW. Initially, the sample is slowly dipped in the pre-heated suspension at speed of 5 μm/s and kept in that position for 2 min (immersion time, t_i) then, the sample is pulled out the SPs suspension at a controlled V_w until the entire sample area is outside the SPs suspension.

2.4. Coating Characterization

1 2 3 4 5 6 7 8 9 10 11 12 13 14 15 16 17 18 19 20 21 22 23 24 25 26 27 28 29 30 31 32 33 34 35 36 37 38 39 40 41 42 43 44 45 46 47 48 49 50 51 52 53 54 55 56 57 58 59 60

After dip-coating, morphological analysis of the SPs coating has been carried out by optical microscopy and scanning electron microscopy (SEM). Optical micrographs are acquired by a digital camera (Leica MC170 HD), using a Nikon optical microscope in reflection mode (objective magnifications ×50 and ×1000). Optical microscopy allows to determine the total surface coverage, and the surface covered by either SPs single layer (SL), SPs multi-layer (ML) or non-assembled SPs. This analysis has been carried out at multiple areas along the coated surface (see **Figure S-2**). The confirmation of each type of coating is demonstrated by SEM. SEM of SPs coatings is performed with a Hitachi S4700 at following operating parameters: 5 kV and 7.4 mm WD. To improve the sample conductivity, an 80-100 Å thin layer of Au is sputtered onto the SPs coated surface.

3. Results and Discussion

Once the substrate is dipped in the SPs suspension, the liquid solvent adheres to the solid substrate surface due to the intermolecular forces between the solvent and hydroxylated Si surface. The capillarity effect pulled the liquid up forming a concave meniscus. The curvature of the meniscus can be described by the contact angle (θ_m) and the radius of curvature (r_{curve}), and depends on the hydrophilicity of the substrate surface (see **Figure S-3**). Analysing *in-situ* the dynamic assembly of SPs on Si substrate during dip-coating experiments carried out at above conditions, we noted the formation of three areas, namely: i) deposition area, ii) assembling area, and iii) collection area as schematically illustrated in the inset of **Figure 2**. The deposition area is a dry region where SPs are attached to the receiver substrate, forming either hexagonal close-compact packed (HCP) crystalline structures with different thickness (SL or ML), or a random dispersion of SPs. In the assembling area, SPs adopt almost the final structure but still are embedded in thin film of solvent, which tends to evaporate at a rate J_E which is mainly function

1
2
3
4
5
6
7
8
9
10
11
12
13
14
15
16
17
18
19
20
21
22
23
24
25
26
27
28
29
30
31
32
33
34
35
36
37
38
39
40
41
42
43
44
45
46
47
48
49
50
51
52
53
54
55
56
57
58
59
60

of T_s. The solvent evaporation leads to downshift the interface formed between deposition and interface areas, at a speed namely V_m (expressed in μm/s), which depends on T_s as will show later on and. Finally, the collection area is a region of the suspension where volumetric density of SPs is higher with respect to the rest of the suspension due to the continuous flux of particles (J_p) produced by the convective forces in the suspension (J_s). The ratio of substrate surface dip-coated by SL, ML and randomly dispersed SPs is analysed as a function of dip-coating conditions, including T_s, V_w, V_m, θ_w and L_w, as well as the SPs diameter, aiming to find the optimum conditions to dip-coat SiO_2 SPs over large-areas for different applications. For the sake of comparison, outcomes obtained from the analysis are summarized in **Table 2**.

3.1. Effect of Suspension Temperature on Dip-coating

Using 1 μm SiO_2 SPs suspension with a SPs concentration of 0.31% w/v, the surface coverage (ϕ) on a 1.5×1.5 cm^2 Si substrate has been analysed by optical microscopy and SEM as a function of T_s. For these experiments, T_s ranging between RT and 80°C have been studied. Keeping the sample completely immersed in the suspension and at a static position, i.e. $V_w = 0$, the evaporation of the solvent (J_E) leads to downshift the meniscus level at a speed of $V_m>0$, which depends on T_s (**Figure 3**(a)).

At RT, the optical microscopic analysis shows only SPs dispersed randomly over the Si substrate surface, i.e. without forming a continuous close-compact layer of SPs. The lack of T_s strongly reduces V_m which results in a wide meniscus shape, i.e. high r_{curve} and θ_m (**Figure S-3**(a)), reducing J_s and then J_p towards the collective area. The low density of SPs at the collection area are the main factor hindering the formation of a SPs SAM at RT. Under the described static conditions, i.e. $V_w = 0$, the formation of a close-compact SL and ML of SPs has been observed for T_s above 50°C (**Figure 3**(a)). This result indicates that the assembly of SPs forming close-

1 2 3 4 5 6 7 8 9 10 11 12 13 14 15 16 17 18 19 20 21 22 23 24 25 26 27 28 29 30 31 32 33 34 35 36 37 38 39 40 41 42 43 44 45 46 47 48 49 50 51 52 53 54 55 56 57 58 59 60

compact crystalline structures is clearly influenced by T_s. For $T_s \geq 50^oC$, we observed the assembly of SiO_2 SPs forming SL, ML and random dispersions over the surface of Si substrate. At $T_s = 50^oC$, the substrate surface is mainly not covered, reaching a total surface coverage (ϕ_T) values of only 34%, with only a small area around ϕ_{SL} = 10.1% covered by a SL (ML formation has not been observed), and the rest of the area (~23.9%) covered by randomly dispersed SPs (ϕ_{SPs}). At $T_s = 60^oC$, the ϕ_T increases up to 48.6%, exhibiting also a slight increase of the SL coverage (ϕ_{SL} = 18.8%), the formation of a continuous ML covering around ϕ_{ML} = 10.9% of the whole area, and a decrease of ϕ_{SPs} down to 18.8%. A higher magnification view of the interface formed between SL and ML is presented in the inset of **Figure 3**(a) where a SEM image taken at that interface shows the clear contrast formed between both regions. The increase of T_s up to 70^oC leads to a significant improvement of the ϕ_T, reaching almost 100% coverage of 1.5×1.5 cm^2 total sample area. In these conditions, ϕ_{SL} and ϕ_{ML} reach values of 80.9% and 19.1%, respectively. However, we observed that a further increase of T_s up to 80^oC hinders the performance of dip-coating by exhibiting a reduction of the ϕ_T, $\phi_{SL,}$ ϕ_{ML} down to 82.2%, 67.2%, and 15.0%, respectively. This reduction of ϕ_{SL} and ϕ_{ML} is occurring because of the non-assembled SPs (ϕ_{SPs}) as observed in **Figure 3**(a). **Table 2** summarizes $\phi_{T,}$ ϕ_{SL}, ϕ_{ML} and ϕ_{SPs} as a function of T_s, excluding the RT conditions (which may not be relevant for this discussion). Standard error of the mean data recorded in **Table 2**, corresponding to a series of at least five experiments performed at each condition. The low dispersion of the obtained ϕ (< ±0.3) confirms the reproducibility of the developed procedure.

The above results prove that T_s has a strong influence on the assembly of SPs on a hydroxylated Si surface (which has a direct effect on ϕ_T) and on the self-assembly process as demonstrated by the formation of both SL and ML. In this regard, we hypothesize that the increase of T_s leads to

the change of the meniscus shape, reducing both θ_m and r_{curve} the intermolecular forces act on the solvent adhered to the substrate surface, elongating the meniscus, and then, reducing both θ_m and r_{curve} (**Figure S3**(b)). This effect is expected to be larger as T_s increases. For the sake of explanation, one can define V_s and V_m, as the downshift speed of the suspension level and meniscus level, respectively, allowing to study the speed of the top part of the meniscus (V_m) which can be different than the total solution level mainly due to the capilarity effect (V_s). The increase of T_s leads to an increase of both V_s and V_m, however, due to a large area exposed to the air, V_s - V_m is expected to be always positive. As the difference between V_s and V_m increases with T_s, the height of the liquid column adhered to the substrate surface increases. In this scenario, the gravity force reduces both θ_m and r_{curve} (see **Figure S-3**(b)), which can contribute to the increase of the SPs flux towards the collection area (J_p).[19, 46] However, an excess of temperature (T_s >80°C) could lead to the deposition of SPs ML at expense of SL (T_s = 80°C in **Figure 3**(a)), mainly due to the accumulation of high density of SPs at the collection area. On the other hand, the less temperature (T_s < 50°C in **Figure 3**(a)) hinders the formation of SiO_2 SPs SL and ML mainly due to the low concentration of SiO_2 SPs at the drying region. All these factors lead to the formation of periodic stripes of SL and ML and reduce ϕ_{SPs} and non-covered areas, which are in good agreement with previous observations.[19, 46] In order to prevent the formation of stripes, and to obtain the deposition of a continuous SPs SL, the use of different withdrawal speeds is investigated in this work.

1
2
3
4
5
6
7
8
9
10
11
12
13
14
15
16
17
18
19
20
21
22
23
24
25
26
27
28
29
30
31
32
33
34
35
36
37
38
39
40
41
42
43
44
45
46
47
48
49
50
51
52
53
54
55
56
57
58
59
60

3.2. Effect of Withdrawal Speed on Dip-coating

It is clear that a simple evaporation of solvent can form SL of SiO_2 SPs on a hydroxylated Si substrate surface at $T_s > 50^oC$. We further investigate the effect of speed of substrate withdrawal on ϕ. For initial V_w we chose to use a speed similar to V_m because we hypothesize that synchronizing both speeds would improve the formation of SPs SAM, i.e. increasing ϕ_T *and* ϕ_{SL} while reducing both ϕ_{ML} and ϕ_{SPs}. The V_w was in the range of 0.1-100 μm/s, which is similar to those reported in the literature for dip-coating of large SiO_2 SPs SAM.[19-20] However, in those experiments the role of J_E (and associated T_s, RH and V_m) was not clearly established. Here, we have experimentally determined the V_m in SPs suspensions (SPs diameter of 1 μm and SPs concentration of 0.31% w/v) as a function of T_s, using an optical microscope and a micrometric scale to measure the shift of the meniscus top-part overtime. These values are mentioned in the last column of **Table 2**. A series of dip-coating experiments were carried out at T_s of 50, 60, 70 and 80°C, using a V_w of 0.37, 0.64, 1.30 and 2.32 μm/s, respectively to obtain V_m at each T_s. The range of V_w used here is 3 orders of magnitude slower than that used by Wang et al.[20] for the room-temperature dip-coating of 2 μm SiO_2 SPs over record-breaking large areas (~0.3 cm^2). However, as we demonstrate that the chosen range of V_w dramatically improves the surface coverage of SPs SAM under temperature-assisted dip-coating conditions.

Comparing the performance of dip-coating processes carried out at $V_w = 0$ (**Figure 3**(a)) and $V_w \neq 0$ (**Figure 3**(b)) we note that the latter clearly shows positive effects on the assembly of SiO_2 SPs at large areas. In the case of RT, we observe an improvement in the ϕ_T reaching values around 23% mainly because the formation of both SL and ML, as well as the attachment of non-assembled SPs. In this case, the solvent evaporation occurs after the whole substrate is outside the SPs suspension. This leads to the formation of evaporation regions with random shapes, i.e.

1 2 3 4 5 6 7 8 9 10 11 12 13 14 15 16 17 18 19 20 21 22 23 24 25 26 27 28 29 30 31 32 33 34 35 36 37 38 39 40 41 42 43 44 45 46 47 48 49 50 51 52 53 54 55 56 57 58 59 60

the deposition interface is not flat as observed in dip-coatings carried out at higher temperatures, promoting the uncontrolled accumulation of SPs at the boundaries of the evaporation regions, resulting in the formation of ML rather than SL. At T_s = 50°C and V_w = 0.37 μm/s, the increase of ϕ_T and ϕ_{SL} up to 56.7% (from 34.0% obtained at V_w = 0) and 56.7% (from 10.1% obtained at V_w = 0), respectively is noted while hindering the attachment of non-assembled SPs, i.e. ϕ_{SPs} ~0. In addition, we observe an improvement in the coverage uniformity over the 1.5×1.5 cm^2 analysed area (**Figure 3**(b)). At T_s = 60°C, the use of a V_w = 0.64 μm/s reduces ϕ_{ML} down to 21.6%, while showing similar ϕ_{SL} of 56.2%. This means there is a slight enhancement of the ϕ_T up to 77.9% with respect to the static conditions (48.6% at V_w = 0). On the other hand, we observe that using T_s = 70°C and V_w = 1.3 μm/s, both ϕ_T and ϕ_{SL} are enhanced and reach values closer to 100% of 1.5×1.5 cm^2 area, whereas the contribution of ML is almost negligible (ϕ_{ML}~0). In contrast, a further increase of the temperature up to T_s = 80°C and using a higher V_w = 2.32 μm/s, results in a high ϕ_T of 98.4%, but showing the formation of small areas consisting of SPs ML (ϕ_{ML} = 0.5%). Last result confirms that the use of an extremely high T_s, even at dynamic conditions (V_w > 0), hinder the formation of SPs SL mainly because: i) the J_p increases at the collection area, and ii) the increase of J_E expands the evaporation area and promotes the formation of ML rather than SL.

Analysing ϕ, the withdrawal of the sample at V_w in the range of V_m has been demonstrated to produce an increase of both ϕ_T and ϕ_{SL}. This result proves that V_w of 1.30 μm/s is a "natural" assembling speed (V_{w0}) at T_s = 70°C for 1 μm SiO_2 SPs and the ambient RT and RH of 20%. To demonstrate this, we further analysed the surface morphology of 1.5×1.5 cm^2 Si substrate dip-coated at T_s = 70°C and using V_w below and above V_{w0} = 1.30 μm/s. The former conditions i.e. $V_w < V_{w0}$ show results similar to those presented in **Figure 3**(a) for T_s = 70°C, where V_m

1 2 3 4 5 6 7 8 9 10 11 12 13 14 15 16 17 18 19 20 21 22 23 24 25 26 27 28 29 30 31 32 33 34 35 36 37 38 39 40 41 42 43 44 45 46 47 48 49 50 51 52 53 54 55 56 57 58 59 60

predominant over V_w promotes the formation of ML and results in a periodic SL and ML stripes. On the other hand, at $V_w > V_{w0}$ we observed a uniform coverage of SPs clusters consisting 2-10 SPs uniformly covering the whole substrate area. These results are in good agreement with previous works,[19] where dip-coating experiments (carried out in similar conditions and using SPs with diameters ranged between 0.21-2.1 μm) conclude that there is a characteristic transition V_w around 2.3 μm/s above what the formation of narrow stripe-like patterns is promoted, and below what the deposition of a continuous SPs SAM can be obtained. In this work, we present for the first time the natural assembling speed for SiO_2 SPs, below the transition V_w,[19] that allows the deposition of SAM over record-breaking large areas around 1.5×1.5 cm^2.

3.3. Effect of Withdrawal Angle on Dip-coating

The gravity has been demonstrated to play a major role in the SPs assembly by dip-coating method mainly because it directly affects curvature of the meniscus. Dip-coating experiments are carried out through vertical withdrawal of the receiver substrate from the SPs solution.[19-20] Here, we have compared the performance of dip-coating experiments carried out at different withdrawal angles, including $\theta_w = 0^o$ (**Figure 4**(a)) and 45° (**Figure 4**(b)), where θ_w is defined as the angle formed between the sample surface and the withdrawal direction (see insets of **Figure 4**). For these experiments, we have used a $T_s = 70^oC$ and $V_w = 1.3$ μm/s and SPs with a diameter of 1 μm. **Figure 4**(a) and (b) show the SEM images of representative areas of samples dip-coated at θ_w of 0° and 45°, respectively. From these figures, one can deduce that θ_w has an important role on the SPs assembly, θ_w of 0° shows better results in terms of large areas coating of SPs SL (see SAM of SiO_2 SPs in the bottom inset of **Figure 4**(a)). In contrast, the at $\theta_w = 45^o$ the formation of defects (i.e. empty areas where SPs are not forming close compact structures) is prominent along with MLs consisting of vertical stacked SPs as highlighted in the bottom inset

of **Figure 4**(b). This behavior can be explained due to local defects existing along the area of the receiver substrate (possibly created during the substrate preparation, see Section 2.2), which may lead to a local variation of the wettability along the substrate area, causing the formation of a non-flat deposition interface in the top part of the meniscus. As illustrated in the insets of **Figure 4**(a, b), the increase of θ_w increases the thickness of the meniscus and this leads to reduced convective flow of SPs towards the evaporation area (low J_p and J_s) and reduces J_E. These both hinder the formation of a continuous SL, while promoting the formation of defects and locally MLs. In contrast, the reduction of θ_w down to 0° decreases the thickness of the meniscus and increases J_E, J_p and J_s which improve the formation of large area SL while lowering the chances of the formation of defects and ML (**Figure 4**(a)).

3.4. Effect of SPs Diameter on Dip-coating

Dip-coating of SPs with diameters ranged between 200 nm to 2 μm has been reported in literature.[20, 29] Here we present an investigation of the effect of SPs size on the dip-coating assembly mechanism including the dip-coating of nanometric SiO_2 SPs (diameter of 100 nm) and in this regards the results in this section are complementary to the previous works. The large-area dip-coating of SPs with different diameters, including 1 μm, 500 nm and 100 nm is thoroughly analysed here for applications that will be presented in the next section. For the sake of comparison, we have used the same suspension concentration of 0.31% w/v independently of the SPs size, and standard dip-coating experimental conditions, i.e. $T_s = 70^oC$, $V_w = 1.3$ μm/s and $\theta_w = 0^o$. **Figure 5** presents SEM images of resulting Si substrate surface morphology after dip-coating experiments carried out using SiO_2 SPs with diameters 1 μm (**Figure 5**(a)), 500 nm (**Figure 5**(b)) and 100 nm (**Figure 5**(c)). From those figures, one can observe that there is: i) a good SL coverage uniformity (100% surface coverage), ii) low defects density, iii) HCP

crystalline structure, and iv) absence of ML and non-assembled SPs regions. Analyzing areas dip-coated by a similar number of SPs (see insets of **Figure 5**), it is observed that statistically the defects are more or less independent of the SPs diameter. Figure S-4 in supporting information shows assembly of the resulting SLs for similar areas dip-coated with SPs of different diameters. The crystallinity of the assembly can be improved by carrying out the process with highly mono-dispersed SPs. As clearly observed in the inset of **Figure 5**(c), by reducing the size of the SPs down to diameters of 100 nm, dip-coating produces grain boundaries between regions with hexagonal close compact structures. From this figure, one can roughly estimate that grains have an average size of around 1 μm^2. Considering a HCP structure, the area covered by a single cell (consisting in 6 SPs) of SPs with a diameter of 100, 500, and 1000 nm is 2.4×10^{-10}, 5.8×10^{-9}, and 1.5×10^{-8} cm^2, respectively. Accordingly, the SAM domain size decreases with the SPs diameter, making more difficult to obtain single domain SAM as the SPs size reduces. The achievement of single domain SAM, preventing the formation of grain boundaries (see inset of **Figure 5**(c)) could strongly affect the performance of SPs coatings for applications such as those presented in this work (see section 3.6). In addition, the huge areal extension obtained with nanometric SiO_2 SPs (diameter of 100 nm) makes the temperature-assisted dip-coating approach presented here, an excellent alternative for the deposition of highly ordered and compact nano-SPs over large areas (**Table 1**).

3.5. Effect of Withdrawal Length on Dip-coating

In previous experiments, the Si substrates were withdrawn at a constant V_w (typically in the μm/s range) until the entire sample is pulled out of the suspension. Due to convective mechanism,[36] the observed SL stripes (see **Figure 3**) is common in large-area dip-coating processes developed in vertical position.[19-20] Here, we demonstrate that both SPs SL stripe width and stripe-to-stripe spacing can be controlled by L_w. This could be a low-cost and rapid process for creating

periodical patterns of SiO_2 micro-SPs SAM, without using complex steps involving lithography or surface functionalization. Since our work presents an effective approach to control SPs stripe width and spacing through V_w and optimizing L_w under the influence of T_s, this result complements previous works such as the one reported by Ghosh et al.[19] where SiO_2 SPs stripe morphology is tuned by V_w. For the sake of simplicity, we have used T_s of 70°C, θ_w of 0°, and a 1 μm SPs suspension with a concentration of 0.31% w/v to investigate the effect of L_w on the resulting dip-coating. To produce stripes of SPs, we increased V_w to 1.3 mm/s, which is three orders of magnitudes faster than the V_m used in continuous dip-coating (**Figure 3**). As demonstrated elsewhere,[19] the use of V_w extremely higher respect to the optimum V_w resulting in continuous SPs SAM promotes As-cleaned Si substrate was vertically dipped in the SPs suspension for t_i of 2 min to allow the formation of the meniscus due to the capillarity and gravity effects (**Figure 6**(a)). Thereafter, the substrate was pulled out of the suspension at V_w = 1.3 mm/s, which led to the formation of two dry and wet regions on top of the substrate surface (**Figure 6**(b)). This can be due to V_m being low in comparison to V_w, which leads to formation of an uncovered region underneath the wet region whose width is similar than L_w. In this regard, we have observed that L_w has a direct effect on the stripe-to-stripe spacing, as demonstrated in **Figure 6**(c-f) where dip-coating experiments carried out at L_w of 1, 0.5, 0.25, and 0.125 mm have been shown to result in periodical patterns of SL SPs with a stripe-to-stripe spacing approximately equal to L_w. Analysing **Figure 6**(c-f), one can conclude that SPs strip width is ranged between 125 and 360 μm and the strip length is mainly limited by the size of the substrate (in this case 1.5 cm). Further exploring the limits of proposed method, we note that $L_w < 0.125$ mm lead to the formation of MLs between stripes, which hinders the use of this technique for the applications presented below.

1
2
3
4
5
6
7
8
9
10
11
12
13
14
15
16
17
18
19
20
21
22
23
24
25
26
27
28
29
30
31
32
33
34
35
36
37
38
39
40
41
42
43
44
45
46
47
48
49
50
51
52
53
54
55
56
57
58
59
60

3.6. Applications

In this section, we show two potential applications of large-area coatings of SiO_2 SPs described above using dip-coating procedure., namely: i) anti-reflective coatings for PV cells,[9] smart-coatings for vehicles, lens of glasses, screens of smart-phones, and ii) SAMs of SPs for nano-sphere lithography (NSL) by forming “inside-out” templates, from SPs SAMs as a sacrificial porous mask for the fabrication of nano-porous metallic films that are utilized, e.g. as catalytic layer during the MACE synthesis of Si NWs.[14] In this regard, first we present the characterization of anti-reflective properties of SiO_2 SPs SAMs, consisting in SPs with different diameters (0.1, 0.5 and 1 μm), and their successful dip-coating on top of a poly-Si PV cell (from Sanyo). This is followed by second application where we show the use of SiO_2 SPs SAMs as sacrificial mask for the deposition of a micro-porous Ag layer on top of a Si wafer and the successful utilization of this Ag layer as catalyst for MACE synthesis of vertically aligned Si NWs.

3.6.1 Anti-reflective Coating for PV cells.

The control and optimization of dip-coating operating parameters, i.e. V_w and T_s, opens interesting avenues for depositing SiO_2 SPs SAM over large areas which can be potentially used as ARC in photovoltaic (PV) cells[9]. Here, we have demonstrated the antireflective properties of a large-area SiO_2 SPs SAM dip-coated on a Si substrate, analysing the effect of different SPs diameters (0.1, 0.5 and 1 μm) on the reflectance (R) of the resulting sample surface. **Figure 7**(a) represents R of a Si wafer (with and without SiO_2 SPs SL coating) as a function of photon wavelength (λ) in the visible range, i.e. $400 < \lambda < 700$ nm. Prior to the dip-coating, Si wafer shows R ranged between 46 and 55%. In contrast, the dip-coating of SiO_2 SPs, forming a SAM on top of the Si wafer surface, is observed to reduce R down to 15-26%. In HCP structures such as those shown in **Figure 5**(a,c,e) for dip-coatings of 1 μm, 500 nm and 100 nm SiO_2 SPs, the

1 2 3 4 5 6 7 8 9 10 11 12 13 14 15 16 17 18 19 20 21 22 23 24 25 26 27 28 29 30 31 32 33 34 35 36 37 38 39 40 41 42 43 44 45 46 47 48 49 50 51 52 53 54 55 56 57 58 59 60

ratio of covered/uncovered areas (see inset of **Figure 7**(a)) results in ~92% (independent on the SPs size). Accordingly, the *R* shows similar values for all dip-coatings developed using SPs with different size (**Figure 7**(a)). The slight variations of *R* observed in **Figure 7**(a) might be due to scattering effects owing to varying SPs size (see inset of **Figure 7**(a)).

For the sake of simplicity, 1 μm SiO_2 SPs are dip-coated on a poly-Si PV cell surface, studying the effect of the coating on the PV cell properties. **Figure 7**(b) and (c) present the current density (J) and power density (P) as a function of the applied voltage (V) of a poly-Si PV cell, respectively, with (coloured in red) and without (coloured in black) the SPs coating. The characterization of the PV cell before and after the SPs coating has been carried out by a AM1.5D (AM: Air Mass) solar simulator with a 100 mW/cm^2 Xe light lamp. From **Figure 7**(b), one can easily conclude that the SPs coating increases the short-circuit current density (J_{sc}) from 24 to 32.2 mA/cm^2, while exhibiting approximately the same open-circuit voltage (V_{oc}) around 0.57-0.58 V. From these characteristics, we have calculated a maximum power density (P_{max}) of 13.7 and 18.7 mW/cm^2, without and with SPs coating, respectively. Then, the efficiency of the solar cell (η) can be estimated using the density of the lamp (100 mW/cm^2), resulting in an enhancement of η around 3% mainly due to the anti-reflective effect of the SPs coating, which can reduce the loss due to direct reflection of light on top of the PV cell surface.[47]

3.6.2 Porous Metallic Coatings for Catalysed NWs Synthesis.

As an alternative application of the large-area SiO_2 SPs dip-coating achieved in this work, we demonstrate using periodic SiO_2 SPs patterns dip-coated on top of a Si substrate as a mask for creating a nano metallic mesh used as catalyst in MACE synthesis of Si NWs.[14] **Figure 8** presents a 3D schematic illustration of MACE fundamental steps, comprising of: (a) dip-coating of SiO_2 SPs over a large-area Si wafer surface (with native oxide); (b) reactive-ion etching (RIE)

1
2
3
4
5
6
7
8
9
10
11
12
13
14
15
16
17
18
19
20
21
22
23
24
25
26
27
28
29
30
31
32
33
34
35
36
37
38
39
40
41
42
43
44
45
46
47
48
49
50
51
52
53
54
55
56
57
58
59
60

of SiO_2 SPs using CHF_3/Ar (25 sccm / 18 sccm), 200 Watt, 30 mT at RT for (b1) 0, (b2) 5, (b3) 8, (b4) 11, (b5) 15, and (b6) 17 min; (c) deposition of 100-200 nm of Ag layer (see SEM image in (c1)); (d) sonication in ethanol for 5 min creating a periodic distribution of micro-holes (see SEM image in (d1)); (e) MACE process dipping the sample in a HF:H_2O_2 solution for 30 min resulting in vertically aligned Si NWs (see SEM image in (e1)).

Initially, 1 μm SiO_2 SPs are dip-coated on top of a 1.5×1.5 cm^2 Si substrate as schematically depicted in **Figure 8**(a) and demonstrated by SEM analysis (**Figure 8**(b1)). Prior to the MACE process, we purposely decrease the initial SPs diameter and increase the SP-to-SP spacing by RIE to achieve NWs with controlled diameter. Resulting SPs diameter and SP-to-SP spacing have been analysed by SEM (**Figure 8**(b1-b6)). **Figure 8**(b7) records average SPs diameter and SP-to-SP spacing obtained from SEM analysis and their corresponding standard deviation as a function of the RIE time. This figure includes experimental data obtained from SEM analysis along with the best fitting corresponding to an exponential function. This method permits us to reduce the initial size of the SPs from 1 μm down to 600 nm which has a direct effect on the diameter of resulting NW during MACE. This also offers a simple way to develop NWs with different diameters to meet the requirements of a target application. Similar RIE process carried out with 500 and 100 nm SPs resulted in continuous SiO_2 SPs SL, comprising SPs diameters from 20 nm to 1 μm. After RIE step, we deposit Ag layer by thermal evaporation. To prevent the formation of a continuous Ag layer on top of the Si substrate its thickness is less the height of assembled SPs **Figure 8**(c1). The discontinuity of the metallic nano mesh is a key feature that allows the successful development of MACE process.[14] Resulting sample is then dipped in ethanol and sonicated for 5 min to remove the SPs from the substrate surface. **Figure 8**(d) shows the SEM image of a resulting porous Ag layer after the sonication step. As mentioned above, the

pore size can be roughly controlled by the initial size of the SPs. Since the Ag thermal evaporation is highly directional, each SP present a mask over the Si substrate surface, slightly increasing the pore size with respect to the SP diameter. Finally, the sample is dipped in a HF:H_2O_2, promoting the preferential etching of Si wafer underneath the Ag layer, and resulting in vertically-aligned Si NWs on top of Si wafer as demonstrated by SEM **Figure 8**(e1). The advanced use of temperature-assisted dip-coating method to create periodic SiO_2 SPs SAM stripes over large areas (**Figure 6**) would allow to control the NW-to-NW spacing resulting from MACE. Therefore, this is a promising low-cost and easy-of-developing approach for improving performance e.g. of transfer-printing of NWs over large areas.[48]

Conclusions

In this work, we have thoroughly analyzed the effect of T_s on the performance of SiO_2 micro- and nano-SPs self-assembled by dip-coating method on large-area Si substrate. For the first time, we have demonstrated the assembly of 100 nm, 500 nm and 1 μm SiO_2 SPs forming a SL hexagonal close packed structure over areas (~2.25 cm^2) which are an order magnitude larger than those reported in literature with sub-micrometric SPs. This is achieved with controled operational parameters such as V_w, θ_w and L_w, and suspension properties including T_s and SPs concentration. From this study, we have confirmed for the first time the key role of the T_s, observing that dip-coating performance of SiO_2 SPs can be improved by syncronizing V_m and V_w. In particular, we have obtained a continous SiO_2 SPs SL over 100% of the 2.25 cm^2 substrate area, using T_s of 70°C, θ_w of 0° (vertical withdrawal), and a V_w of 1.3 μm/s, improve 10 times the performance obtained by room-tempreature dip-coating.[19-20] Through an easy and rapid dip-coating method, we have found a novel approach for creating periodic SiO_2 SPs SL stripes, with excellent dimensional control (i.e. width and spacing between stripes), which can be an low-cost

1
2
3
4
5
6
7
8
9
10
11
12
13
14
15
16
17
18
19
20
21
22
23
24
25
26
27
28
29
30
31
32
33
34
35
36
37
38
39
40
41
42
43
44
45
46
47
48
49
50
51
52
53
54
55
56
57
58
59
60

and high-performance method for the development of optical gratings, filters, polarizers etc. Moreover, the approach has been succesfully used to create uniform and large-area coatings based on SiO_2 SPs for different applications, including ARC on PV cells, and metallic nano mesh for large-area MACE synthesis of vertically aligned Si NWs.

Supporting information

Contact angle measurements of receiver substrate before and after the hydroxylation; Description of the method used to characterize the surface coverage obtained by dip-coating; Schematic illustrations of meniscus shape as a function of the receiver substrate properties.

1
2
3
4
5
6
7
8
9
10
11
12
13
14
15
16
17
18
19
20
21
22
23
24
25
26
27
28
29
30
31
32
33
34
35
36
37
38
39
40
41
42
43
44
45
46
47
48
49
50
51
52
53
54
55
56
57
58
59
60

Figures

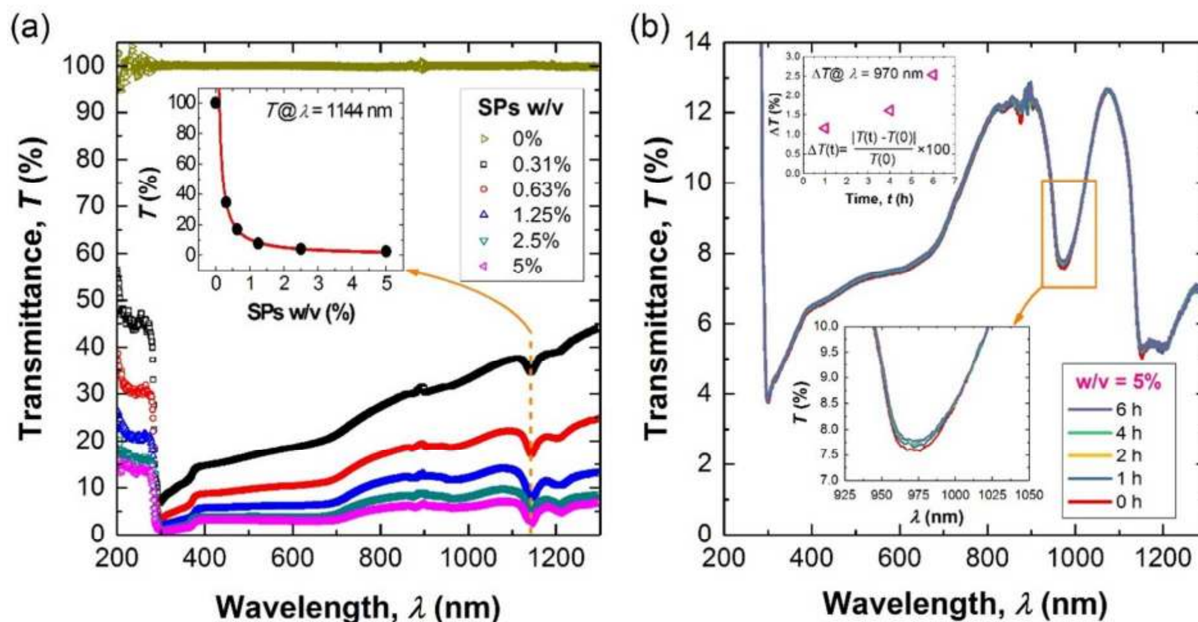

Figure 1. Optical transmittance (T) of 0.5 μm SPs suspension. (a) T vs λ for different SPs w/v%; inset: experimental data and fitting of T vs SPs w/v% @ λ = 1144 nm. (b) T vs λ measured overtime @ w/v of 5%; inset: ΔT overtime @ λ = 970 nm.

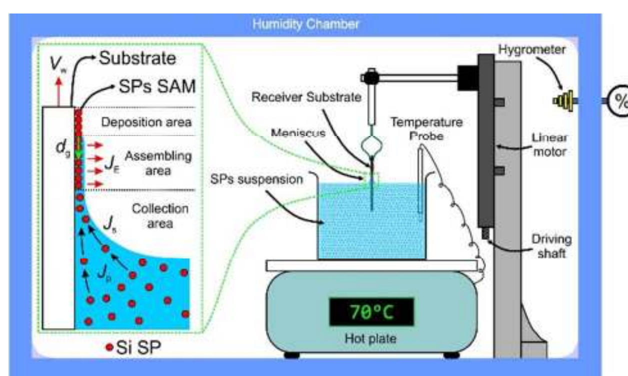

Figure 2. 2D schematic illustration of dip-coating setup. Inset: self-assembly process of SiO_2 SPs driven by dip-coating.

1
2
3
4
5
6
7
8
9
10
11
12
13
14
15
16
17
18
19
20
21
22
23
24
25
26
27
28
29
30
31
32
33
34
35
36
37
38
39
40
41
42
43
44
45
46
47
48
49
50
51
52
53
54
55
56
57
58
59
60

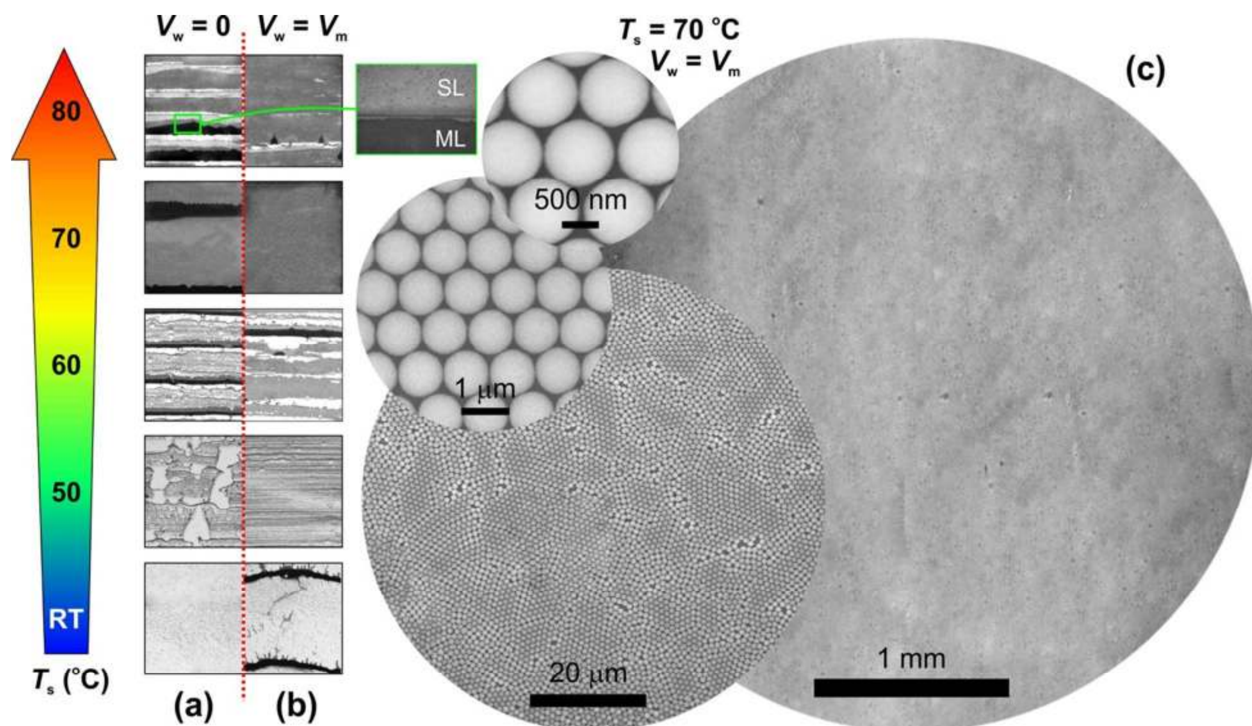

Figure 3. Optical characterization of 1 μm SiO_2 SPs dip-coated on 1.5×1.5 cm^2 Si substrates at RT < T_s < 80 ^oC using V_w of (a) 0 and (b) V_m. Inset: SEM image of SL/ML interface. (c) SEM images of SiO_2 SPs SAM formed at 70 ^oC and V_w of V_m.

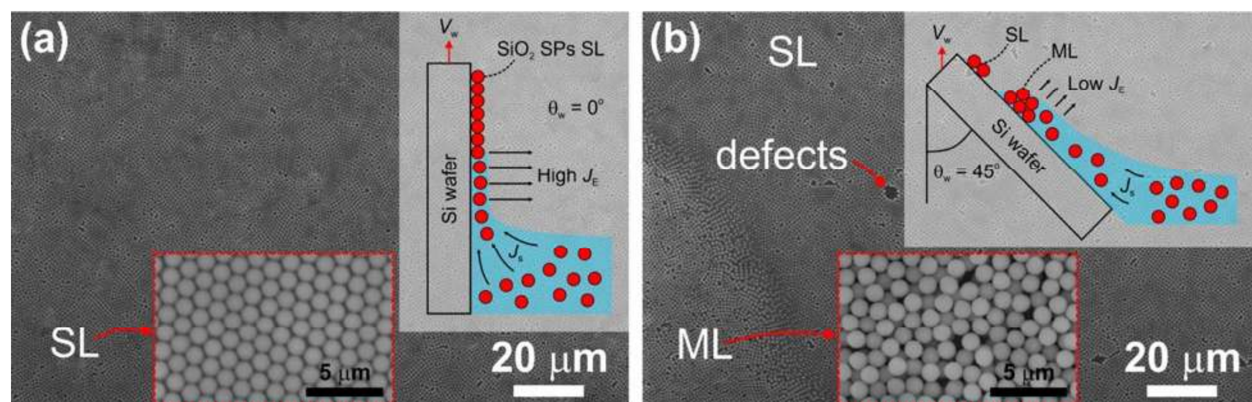

Figure 4. SEM images of dip-coating experiments carried out at θ_w of (a) 0° and (b) 45°. Insets: 2D schematic illustrations of the dip-coating conditions (top-right), higher magnification SEM images of SL and ML regions (bottom).

1
2
3
4
5
6
7
8
9
10
11
12
13
14
15
16
17
18
19
20
21
22
23
24
25
26
27
28
29
30
31
32
33
34
35
36
37
38
39
40
41
42
43
44
45
46
47
48
49
50
51
52
53
54
55
56
57
58
59
60

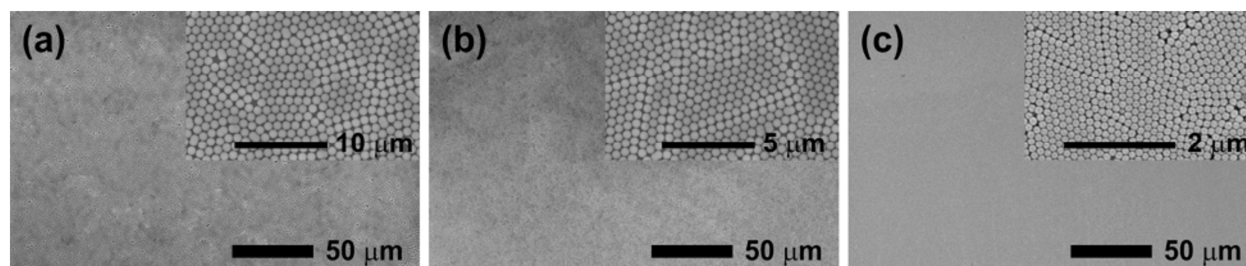

Figure 5. SEM images of Si substrate surface dip-coated with SiO_2 SPs of different diameters, comprising (a) 1 μm, (b) 500 nm, and (c) 100 nm, using T_s = 70°C, V_w = 1.3 μm/s and a suspension concentration of 0.31% w/v. Insets: higher magnified SEM images of SiO_2 SLs.

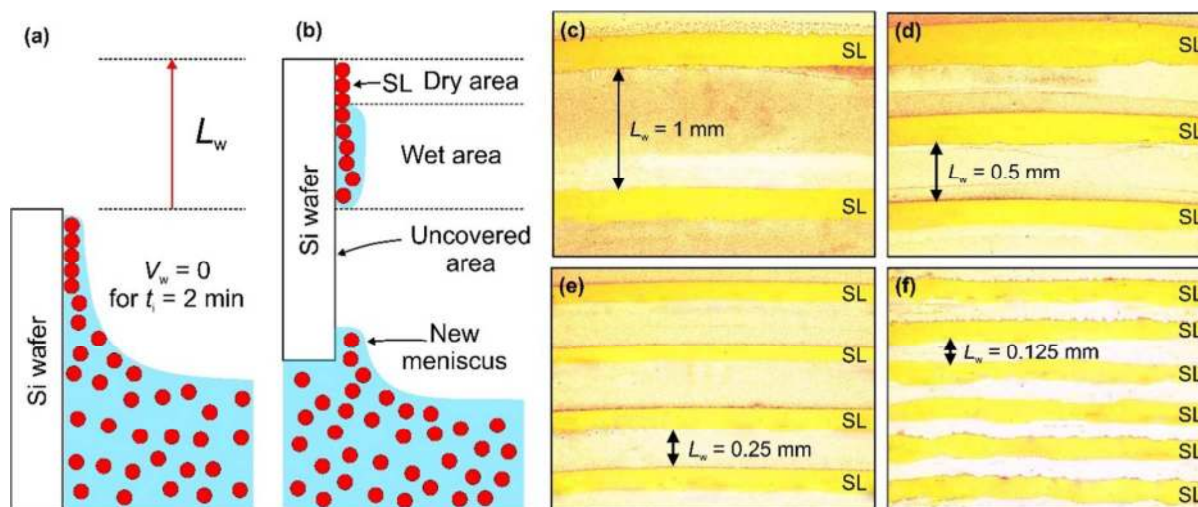

Figure 6. (a, b) 2D schematic illustration of 1 μm SPs based stripes formed by dip-coating procedures carried out at T_s = 70°C, V_w = 1.3 μm/s, θ_w = 0° and L_w of (c) 1 mm, (d) 0.5 mm, (e) 0.25 mm, and (f) 0.125 mm.

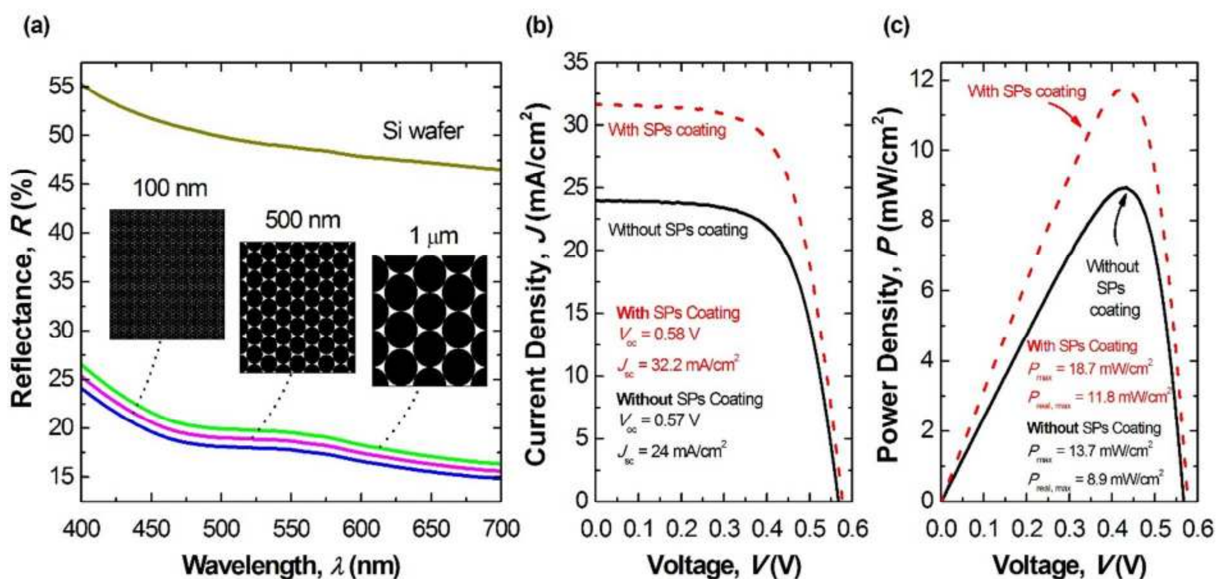

Figure 7. (a) R vs λ of a Si wafer before and after dip-coating of SiO_2 SPs with different diameters; inset: 2D schematic illustrations of areas dip-coated with SPs of different sizes. (b) J-V and (c) P-V of a poly-Si PV cell with and without 1 μm SiO_2 SPs anti-reflective coating; inset: PV cell characteristics.

1
2
3
4
5
6
7
8
9
10
11
12
13
14
15
16
17
18
19
20
21
22
23
24
25
26
27
28
29
30
31
32
33
34
35
36
37
38
39
40
41
42
43
44
45
46
47
48
49
50
51
52
53
54
55
56
57
58
59
60

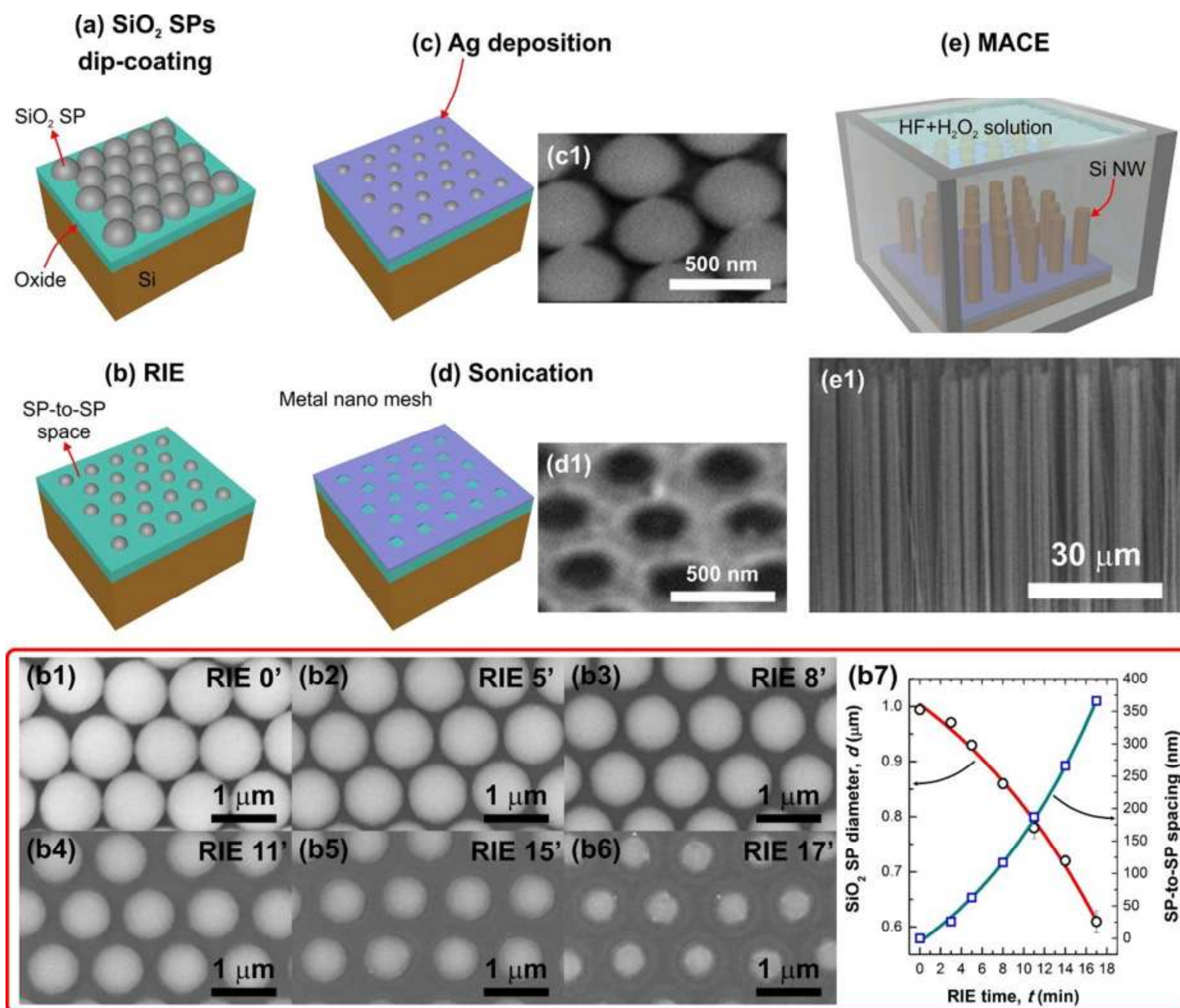

Figure 8. 3D schematic illustration of MACE steps for the synthesis of Si NWs, comprising of: (a) dip-coating of SiO_2 SPs over a large-area Si wafer surface (with native oxide); (b) reactive-ion etching (RIE) of SiO_2 SPs using CHF_3/Ar (25 sccm / 18 sccm), 200 Watt, 30 mT at RT for (b1) 0, (b2) 5, (b3) 8, (b4) 11, (b5) 15, and (b6) 17 min; (b7) SPs size and SP-to-SP spacing vs RIE time; (c) deposition of 100-200 nm of Ag layer (see SEM image in (c1)); (d) sonication in isopropanol for 5 min creating a periodic metallic nano mesh (see SEM image in (d1)); (e) MACE process dipping the sample in a HF:H_2O_2 solution for 30 min resulting in vertically aligned Si NWs (see SEM image in (e1)).

1
2
3
4
5
6
7
8
9
10
11
12
13
14
15
16
17
18
19
20
21
22
23
24
25
26
27
28
29
30
31
32
33
34
35
36
37
38
39
40
41
42
43
44
45
46
47
48
49
50
51
52
53
54
55
56
57
58
59
60

Tables

Table 1. Comparison of various micro- and nano-SPs assembly approaches.

SPs Material	SPs Concentration	SPs Size [μm]	Receiver Substrate	Assembly Technique	Max. SAM coverage [cm^2]	REF [#]
Silica	2.85-3.75% wt.	1.43	Glass, PET, PVC	Charge-reversible substrates	64	[18]
Silica	16.7 mg/ml	0.36, 0.55	Glass	Langmuir-Blodgett	63	[24]
Silica	0.2% wt	0.4	PET	Scalable Printing	30	[33]
Silica	9, 20% wt	0.3, 0.55	Sapphire	Spin-coating	20.3	[22]
Polystyrene	0.5% wt	1.59	Glass	Capillarity Forces	10	[31]
Silica and Latex	35% vol.	0.44	Glass	Spin-coating	6.25	[23]
Au	0.01-0.3% vol.	0.01, 0.015	Glass	Two-plates assisted coating	6.19	[37]
Polystyrene	30 mg/mL	1.4	Glass	Capillary Forces	6	[31]
Polystyrene	0.9-35% vol.	1.1	Glass	Two-plates assisted coating	4	[37]
Silica	5%	0.1, 0.5, 1	Si	Dip-coating	2.25	this work
Polystyrene	0.2-2.5% wt	0.97	Glass	Gravity-assisted convective assembly	2	[30]
Latex	0.8-7.0% wt	0.18-1.15	Glass, Si	Inclined drop-casted method	1.25	[21]
Polystyrene	0.5% wt	0.26-0.6	Glass	Confined Convective Assembly	1	[28]
Latex	1.2% wt	0.32	Glass	Vertical Deposition	1	[32]
Silica and Latex	0.5% vol.	0.7-1.4	Glass	Dielectrophoresis	1	[34]
Silica	5-27	2	Silicon	Dip-coating	0.3	[20]
Silica	5-27	2	Glass	Dip-coating	0.165	[20]
Silica	0.01-0.1	0.21-2.1	Silicon	Dip-coating	0.25	[19]
Polystyrene	1% vol.	0.079-2.11	Glass	Continuous Convective Assembly	0.0006	[29]
Polymer	0.1-0.2 g/mL	1-2.31	Glass	Langmuir-Blodgett	0.00045	[25]

1 2 3 4 5 6 7 8 9 10 11 12 13 14 15 16 17 18 19 20 21 22 23 24 25 26 27 28 29 30 31 32 33 34 35 36 37 38 39 40 41 42 43 44 45 46 47 48 49 50 51 52 53 54 55 56 57 58 59 60

Table 2. Surface coverages of single layer (ϕ_{SL}), multi-layer (ϕ_{ML}) or non-assembled SPs (ϕ_{SPs}) obtained at V_w = 0. In brackets, ϕ corresponding to $V_w = V_m$.

T_s (°C)	ϕ_{SL} (%)	ϕ_{ML} (%)	ϕ_{SPs} (%)	ϕ_T (%)	V_w (μm/s)
50	10.1 (56.7) ±0.1	0 (0)	23.9 (0) ±0.1	34.0 (56.7) ±0.2	0.37
60	18.8 (56.2) ±0.2	10.9 (21.6) ±0.2	18.8 (0) ±0.1	48.6 (77.9) ±0.1	0.64
70	80.9 (100) ±0.1	19.1 (0) ±0.3	0 (0)	100.0 (100) ±0.3	1.30
80	67.2 (97.9) ±0.1	15.0 (0.5) ±0.1	0 (0)	82.2 (98.4) ±0.1	2.32

Corresponding Author

*Prof. Ravinder Dahiya (Ravinder.Dahiya@glasgow.ac.uk)

Bendable Electronics and Sensing Technologies (BEST) Group

School of Engineering, University of Glasgow, United Kingdom (UK)

Authors

Carlos García Núñez (carlos.garcianunez@glasgow.ac.uk)

William Taube Navaraj (w.navaraj.1@research.gla.ac.uk)

Fengyuan Liu (f.liu.1@research.gla.ac.uk)

Dhayalan Shakthivel (Dhayalan.Shakthivel@glasgow.ac.uk)

Ravinder Dahiya (Ravinder.Dahiya@glasgow.ac.uk)

1
2
3
4
5
6
7
8
9
10
11
12
13
14
15
16
17
18
19
20
21
22
23
24
25
26
27
28
29
30
31
32
33
34
35
36
37
38
39
40
41
42
43
44
45
46
47
48
49
50
51
52
53
54
55
56
57
58
59
60

Author Contributions

WTN and RD conceptualized the work. CGN carried out the experiments and characterizations. WTN and DS support CGN for the synthesis of nanowires. CGN wrote the manuscript with support from rest of co-authors. RD provided overall supervision for the project. CGN and WTN made equal contribution.

Funding Sources

This work was supported by the EPSRC Engineering Fellowship for Growth – PRINTSKIN (EP/M002527/1).

Acknowledgment

This work was supported by the EPSRC Engineering Fellowship for Growth – PRINTSKIN (EP/M002527/1). Authors are thankful to Prof. D. Gregory and Mr. D. Cappelluti from School of Chemistry (University of Glasgow) for optical characterization, and Prof. D. Paul and Mrs. L. Ferre from School of Engineering (University of Glasgow) for PV cell characterization.

1
2
3
4
5
6
7
8
9
10
11
12
13
14
15
16
17
18
19
20
21
22
23
24
25
26
27
28
29
30
31
32
33
34
35
36
37
38
39
40
41
42
43
44
45
46
47
48
49
50
51
52
53
54
55
56
57
58
59
60

References

(1) Cebeci, F. Ç.; Wu, Z.; Zhai, L.; Cohen, R. E.; Rubner, M. F. Nanoporosity-driven superhydrophilicity: a means to create multifunctional antifogging coatings. *Langmuir* **2006,** *22* (6), 2856-2862.

(2) Zhang, G.; Wang, D.; Gu, Z.-Z.; Möhwald, H. Fabrication of superhydrophobic surfaces from binary colloidal assembly. *Langmuir* **2005,** *21* (20), 9143-9148.

(3) Naqshbandi, M.; Canning, J.; Gibson, B. C.; Nash, M. M.; Crossley, M. J. Room temperature self-assembly of mixed nanoparticles into photonic structures. *Nature Communications* **2012,** *3*, ncomms2182.

(4) Canning, J.; Ma, M.; Gibson, B. C.; Shi, J.; Cook, K.; Crossley, M. J. Highly ordered mesoporous silica microfibres produced by evaporative self-assembly and fracturing. *Optical Materials Express* **2013,** *3* (12), 2028-2036.

(5) Yamada, Y.; Tadokoro, H.; Naqshbandi, M.; Canning, J.; Crossley, M. J.; Suenobu, T.; Fukuzumi, S. Nanofabrication of a Solid-State, Mesoporous Nanoparticle Composite for Efficient Photocatalytic Hydrogen Generation. *ChemPlusChem* **2016,** *81* (6), 521-525.

(6) Canning, J.; Weil, H.; Naqshbandi, M.; Cook, K.; Lancry, M. Laser tailoring surface interactions, contact angles, drop topologies and the self-assembly of optical microwires. *Optical Materials Express* **2013,** *3* (2), 284-294.

(7) Lu, Y.; Yin, Y.; Li, Z.-Y.; Xia, Y. Colloidal crystals made of polystyrene spheroids: fabrication and structural/optical characterization. *Langmuir* **2002,** *18* (20), 7722-7727.

(8) Knight, J. C.; Broeng, J.; Birks, T. A.; Russell, P. S. J. Photonic band gap guidance in optical fibers. *Science* **1998,** *282* (5393), 1476-1478.

(9) Prevo, B. G.; Hon, E. W.; Velev, O. D. Assembly and characterization of colloid-based antireflective coatings on multicrystalline silicon solar cells. *Journal of Materials Chemistry* **2007,** *17* (8), 791-799.

(10) Jonsson, A.; Roos, A.; Jonson, E. K. The effect on transparency and light scattering of dip coated antireflection coatings on window glass and electrochromic foil. *Solar Energy Materials and Solar Cells* **2010,** *94* (6), 992-997.

(11) Cassagneau, T.; Caruso, F. Inverse opals for optical affinity biosensing. *Advanced Materials* **2002,** *14* (22), 1629-1633.

(12) García-Vidal, F. J.; Pendry, J. Collective theory for surface enhanced Raman scattering. *Physical Review Letters* **1996,** *77* (6), 1163.

(13) Huang, M. H.; Wu, Y.; Feick, H.; Tran, N.; Weber, E.; Yang, P. Catalytic growth of zinc oxide nanowires by vapor transport. *Advanced Materials* **2001,** *13* (2), 113-116.

(14) Zhang, M.-L.; Peng, K.-Q.; Fan, X.; Jie, J.-S.; Zhang, R.-Q.; Lee, S.-T.; Wong, N.-B. Preparation of large-area uniform silicon nanowires arrays through metal-assisted chemical etching. *The Journal of Physical Chemistry C* **2008,** *112* (12), 4444-4450.

(15) Velev, O. D.; Kaler, E. W. Structured porous materials via colloidal crystal templating: from inorganic oxides to metals. *Advanced Materials* **2000,** *12* (7), 531-534.

(16) Ebbesen, T. W.; Lezec, H. J.; Ghaemi, H.; Thio, T.; Wolff, P. Extraordinary optical transmission through sub-wavelength hole arrays. *Nature* **1998,** *391* (6668), 667-669.

(17) Lezec, H. J.; Degiron, A.; Devaux, E.; Linke, R.; Martin-Moreno, L.; Garcia-Vidal, F.; Ebbesen, T. Beaming light from a subwavelength aperture. *Science* **2002,** *297* (5582), 820-822.

(18) Weng, J.; Li, X.; Guan, Y.; Zhu, X.; Zhang, Y. Facile assembly of large-area 2D microgel colloidal crystals using charge-reversible substrates. *Langmuir* **2016,** *32* (48), 12876-12884.

(19) Ghosh, M.; Fan, F.; Stebe, K. J. Spontaneous Pattern Formation by Dip Coating of Colloidal Suspensions on Homogeneous Surfaces. *Langmuir* **2007,** *23* (4), 2180-2183, DOI: 10.1021/la062150e.

(20) Wang, Y.; Chen, L.; Yang, H.; Guo, Q.; Zhou, W.; Tao, M. *Large-area self assembled monolayers of silica microspheres formed by dip coating*; DTIC Document: 2010.

(21) Retsch, M.; Zhou, Z.; Rivera, S.; Kappl, M.; Zhao, X. S.; Jonas, U.; Li, Q. Fabrication of Large-Area, Transferable Colloidal Monolayers Utilizing Self-Assembly at the Air/Water Interface. *Macromolecular Chemistry and Physics* **2009,** *210* (3-4), 230-241, DOI: 10.1002/macp.200800484.

(22) Ogi, T.; Modesto-Lopez, L. B.; Iskandar, F.; Okuyama, K. Fabrication of a large area monolayer of silica particles on a sapphire substrate by a spin coating method. *Colloids and Surfaces A: Physicochemical and Engineering Aspects* **2007,** *297* (1), 71-78.

(23) Mihi, A.; Ocaña, M.; Míguez, H. Oriented Colloidal-Crystal Thin Films by Spin-Coating Microspheres Dispersed in Volatile Media. *Advanced Materials* **2006,** *18* (17), 2244-2249, DOI: 10.1002/adma.200600555.

(24) Szekeres, M.; Kamalin, O.; Schoonheydt, R. A.; Wostyn, K.; Clays, K.; Persoons, A.; Dékány, I. Ordering and optical properties of monolayers and multilayers of silica spheres deposited by the Langmuir–Blodgett method. *Journal of Materials Chemistry* **2002,** *12* (11), 3268-3274.

(25) Lenzmann, F.; Li, K.; Kitai, A.; Stover, H. Thin-film micropatterning using polymer microspheres. *Chemistry of Materials* **1994,** *6* (2), 156-159.

(26) Meng, X.; Qiu, D. Gas-flow-induced reorientation to centimeter-sized two-dimensional colloidal single crystal of polystyrene particle. *Langmuir* **2014,** *30* (11), 3019-3023.

(27) Zhu, J.; Li, M.; Rogers, R.; Meyer, W. Crystallization of hard-sphere colloids in microgravity. *Nature* **1997,** *387* (6636), 883.

(28) Kim, M. H.; Im, S. H.; Park, O. O. Rapid Fabrication of Two- and Three-Dimensional Colloidal Crystal Films via Confined Convective Assembly. *Advanced Functional Materials* **2005,** *15* (8), 1329-1335, DOI: 10.1002/adfm.200400602.

(29) Dimitrov, A. S.; Nagayama, K. Continuous convective assembling of fine particles into two-dimensional arrays on solid surfaces. *Langmuir* **1996,** *12* (5), 1303-1311.

(30) Ye, R.; Ye, Y.-H.; Zhou, Z.; Xu, H. Gravity-Assisted Convective Assembly of Centimeter-Sized Uniform Two-Dimensional Colloidal Crystals. *Langmuir* **2013,** *29* (6), 1796-1801, DOI: 10.1021/la3040227.

(31) Sun, J.; Tang, C.-j.; Zhan, P.; Han, Z.-l.; Cao, Z.-S.; Wang, Z.-L. Fabrication of centimeter-sized single-domain two-dimensional colloidal crystals in a wedge-shaped cell under capillary forces. *Langmuir* **2010,** *26* (11), 7859-7864.

(32) Goldenberg, L. M.; Wagner, J.; Stumpe, J.; Paulke, B.-R.; Görnitz, E. Ordered arrays of large latex particles organized by vertical deposition. *Langmuir* **2002,** *18* (8), 3319-3323.

(33) Jeong, S.; Hu, L.; Lee, H. R.; Garnett, E.; Choi, J. W.; Cui, Y. Fast and scalable printing of large area monolayer nanoparticles for nanotexturing applications. *Nano letters* **2010,** *10* (8), 2989-2994.

(34) Lumsdon, S. O.; Kaler, E. W.; Williams, J. P.; Velev, O. D. Dielectrophoretic assembly of oriented and switchable two-dimensional photonic crystals. *Applied Physics Letters* **2003,** *82* (6), 949-951.

(35) Park, S. H.; Qin, D.; Xia, Y. Crystallization of mesoscale particles over large areas. *Advanced Materials* **1998,** *10* (13), 1028-1032.

1
2
3
4
5
6
7
8
9
10
11
12
13
14
15
16
17
18
19
20
21
22
23
24
25
26
27
28
29
30
31
32
33
34
35
36
37
38
39
40
41
42
43
44
45
46
47
48
49
50
51
52
53
54
55
56
57
58
59
60

(36) Denkov, N.; Velev, O.; Kralchevski, P.; Ivanov, I.; Yoshimura, H.; Nagayama, K. Mechanism of formation of two-dimensional crystals from latex particles on substrates. *Langmuir* **1992,** *8* (12), 3183-3190.
(37) Prevo, B. G.; Velev, O. D. Controlled, rapid deposition of structured coatings from micro- and nanoparticle suspensions. *Langmuir* **2004,** *20* (6), 2099-2107.
(38) García Núñez, C.; Taube, W.; Polat, E. O.; Dahiya, R. Energy-Autonomous, Flexible, and Transparent Tactile Skin. *Advanced Functional Materials* **2017,** *27* (18), 1606287-n/a, DOI: 10.1002/adfm.201606287.
(39) Yogeswaran, N.; Dang, W.; Navaraj, W. T.; Shakthivel, D.; Khan, S.; Polat, E. O.; Gupta, S.; Heidari, H.; Kaboli, M.; Lorenzelli, L. New materials and advances in making electronic skin for interactive robots. *Advanced Robotics* **2015,** *29* (21), 1359-1373.
(40) Taube Navaraj, W.; García Núñez, C.; Shakthivel, D.; Vinciguerra, V.; Labeau, F.; Gregory, D. H.; Dahiya, R. Nanowire FET Based Neural Element for Robotic Tactile Sensing Skin. *Frontiers in Neuroscience* **2017,** *11* (501), DOI: 10.3389/fnins.2017.00501.
(41) Dang, W.; Vinciguerra, V.; Lorenzelli, L.; Dahiya, R. Printable stretchable interconnects. *Flexible and Printed Electronics* **2017,** *2* (1), 013003.
(42) Dahiya, R.; Gottardi, G.; Laidani, N. PDMS residues-free micro/macrostructures on flexible substrates. *Microelectronic Engineering* **2015,** *136* (Supplement C), 57-62, DOI: https://doi.org/10.1016/j.mee.2015.04.037.
(43) Fang, H.; Zhao, J.; Yu, K. J.; Song, E.; Farimani, A. B.; Chiang, C.-H.; Jin, X.; Xue, Y.; Xu, D.; Du, W. Ultrathin, transferred layers of thermally grown silicon dioxide as biofluid barriers for biointegrated flexible electronic systems. *Proceedings of the National Academy of Sciences* **2016,** *113* (42), 11682-11687.
(44) Ko, H. C.; Shin, G.; Wang, S.; Stoykovich, M. P.; Lee, J. W.; Kim, D. H.; Ha, J. S.; Huang, Y.; Hwang, K. C.; Rogers, J. A. Curvilinear electronics formed using silicon membrane circuits and elastomeric transfer elements. *Small* **2009,** *5* (23), 2703-2709.
(45) Shoubhik Gupta; William Taube Navaraj; Leandro Lorenzelli; Dahiya, R. Ultra-Thin Chips for High-Performance Flexible Electronics. *npj Flexible Electronics* **2017**.
(46) Abkarian, M.; Nunes, J.; Stone, H. A. Colloidal crystallization and banding in a cylindrical geometry. *Journal of the American Chemical Society* **2004,** *126* (19), 5978-5979.
(47) Arnold, J. W.; Brewer, T. L.; Punyakumleard, S., Anti-reflective coating. Google Patents: 1990.
(48) Fan, Z.; Ho, J. C.; Jacobson, Z. A.; Yerushalmi, R.; Alley, R. L.; Razavi, H.; Javey, A. Wafer-scale assembly of highly ordered semiconductor nanowire arrays by contact printing. *Nano letters* **2008,** *8* (1), 20-25.

1 2 3 4 5 6 7 8 9 10 11 12 13 14 15 16 17 18 19 20 21 22 23 24 25 26 27 28 29 30 31 32 33 34 35 36 37 38 39 40 41 42 43 44 45 46 47 48 49 50 51 52 53 54 55 56 57 58 59 60

TOC Figure